

# Azonia-Naphthalene: A Cationic Hydrophilic Building Block for Stable N-Type Organic Mixed Ionic-Electronic Conductors\*\*

Zhen Huang<sup>+</sup>, Peiyun Li<sup>+</sup>, Yuqiu Lei, Xin-Yu Deng, Yu-Nan Chen, Shuangyan Tian, Xiran Pan, Xun Lei, Cheng Song, Yuting Zheng, Jie-Yu Wang, Zhi Zhang,\* and Ting Lei\*

**Abstract:** Conjugated polymers that can efficiently transport both ionic and electronic charges have broad applications in next-generation optoelectronic, bioelectronic, and energy storage devices. To date, almost all the conjugated polymers have hydrophobic backbones, which impedes efficient ion diffusion/transport in aqueous media. Here, we design and synthesize a novel hydrophilic polymer building block, 4a-azonia-naphthalene (AN), drawing inspiration from biological systems. Because of the strong electron-withdrawing ability of AN, the AN-based polymers show typical n-type charge transport behaviors. We find that cationic aromatics exhibit strong cation- $\pi$  interactions, leading to smaller  $\pi$ - $\pi$  stacking distance, interesting ion diffusion behavior, and good morphology stability. Additionally, AN enhances the hydrophilicity and ionic-electronic coupling of the polymer, which can help to improve ion diffusion/injection speed, and operational stability of organic electrochemical transistors (OECTs). The integration of cationic building blocks will undoubtedly enrich the material library for high-performance n-type conjugated polymers.

## Introduction

Organic materials that can couple ions and holes/electrons transport, also known as organic mixed ionic-electronic conductors (OMIECs), have attracted increasing interest

because they are crucial for applications ranging from healthcare, optoelectronic to energy storage applications.<sup>[1–5]</sup> Organic electrochemical transistors (OECTs) that utilize OMIEC<sup>[6]</sup> as the active layer, are receiving increasing attention due to their high transconductance, low operating voltage (<1 V) and good biocompatibility, making them ideal for biosensing applications. However, most conjugated polymers with alkyl side chains are hydrophobic, and therefore, ion transport in an aqueous medium is challenging. After introducing ethylene glycol (EG) side chains, conjugated polymers become hydrophilic, making ions and electrons transport much more efficiently in water.<sup>[7]</sup> Till now, a number of p-type OECT materials with very good OECT performance parameters have been developed.<sup>[8–14]</sup> For high-performance p-type OECT polymers, like Poly(3,4-ethylenedioxythiophene) (PEDOT)<sup>[13–15]</sup> and Poly(glycolated thiophene-thienothiophene) (p(g2T-TT)),<sup>[10,16]</sup> small building blocks (e.g., thiophene) and electron-donating functional groups (e.g., methoxyl- or ether group) are often used. However, stable n-type OECT materials have not been reported with these blocks.<sup>[17–20]</sup> Generally agreed, the lowest unoccupied molecular orbital (LUMO) energy level dictates the n-type performance. To lower the LUMO energy levels of n-type polymers, large fused heterocyclic aromatics (e.g., naphthalene diimide (NDI),<sup>[20–22]</sup> 7,7'-diazaisoindigo (AIG),<sup>[23]</sup> bithiophene imide (BTI),<sup>[24–26]</sup> pyrazine-flanked diketopyrrolopyrrole (PzDPP),<sup>[27]</sup> benzodifurandione-based oligo(p-phenylene vinylene) (BDOPV)<sup>[28–29]</sup>) and electron-withdrawing functional groups (e.g., F or CN) are frequently used. However, these neutral backbones with fused aromatics are large hydrophobic moieties, and the presence of functional groups (F or CN) further increases the hydrophobicity.<sup>[30]</sup> In addition, these conventional electron-withdrawing groups (e.g., F or CN) cannot efficiently lower the LUMO energy levels. As a result, n-type conjugated polymers are still undeveloped with respect to their p-type counterparts.<sup>[17–20]</sup> The poor n-type OECT performance and device stability greatly limit the applications of OECT devices in complementary-like logic circuits and the improvement of the sensitivity of OECT-based biosensors.<sup>[18,31]</sup> Therefore, it is indispensable and imperative to develop new building blocks for n-type OMIEC materials.

Biological systems work in water through various types of intermolecular interactions. For example, ethidium bromide (EB) is often used as the dye for DNA labeling (Figure 1a).<sup>[32]</sup> Previous studies have demonstrated that the cationic EB molecule can form strong cation- $\pi$  interactions

[\*] Z. Huang,<sup>+</sup> P. Li,<sup>+</sup> X.-Y. Deng, S. Tian, X. Pan, X. Lei, Y. Zheng, Dr. Z. Zhang, Prof. T. Lei  
 Key Laboratory of Polymer Chemistry and Physics of Ministry of Education, School of Materials Science and Engineering, Peking University  
 Beijing 100871 (China)  
 E-mail: zhizhang@pku.edu.cn  
 tinglei@pku.edu.cn

Z. Huang,<sup>+</sup> Y.-N. Chen, Prof. J.-Y. Wang  
 College of Chemistry and Molecular Engineering, Peking University  
 Beijing 100871 (China)

Y. Lei, C. Song  
 College of Engineering, Peking University  
 Beijing 100871 (China)

[†] These authors contributed equally to this work.

[\*\*] A previous version of this manuscript has been deposited on a preprint server (<https://doi.org/10.21203/rs.3.rs-2750943/v1>).

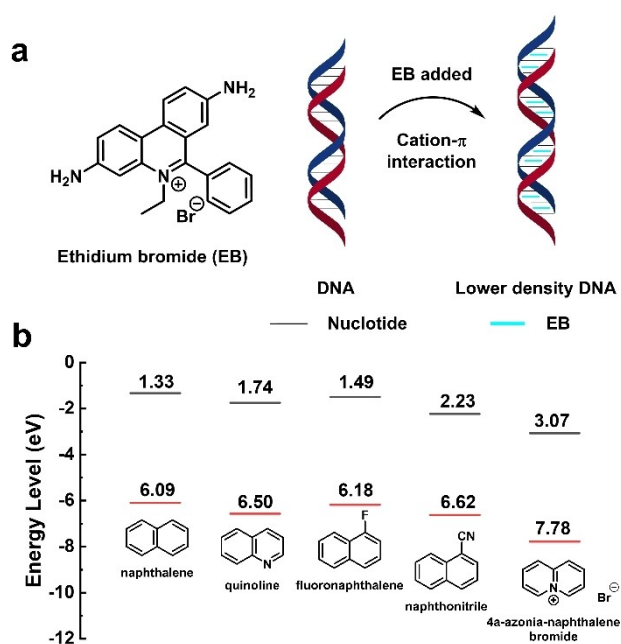


**Figure 1.** Design consideration of the cationic building block. a) The insertion of the cationic molecule, EB, into DNA, where cation- $\pi$  interaction plays a major role. b) Calculated energy levels of naphthalene, quinoline, fluoronaphthalene, naphthonitrile, and azonia-naphthalene (AN) bromide.

with nucleotides.<sup>[33]</sup> Inspired by the cation- $\pi$  interactions in biological systems, here we report the design and synthesis of a cationic polymer building block, 4a-azonia-naphthalene (AN, or quinolizin-5-ium) bromide, for n-type OMIECs. The cationic AN exhibits much stronger electron-withdrawing properties than conventional electron-deficient group (e.g., F or CN) functionalized moieties, yielding n-type polymers with low LUMO energy levels (Figure 1b). We find that the AN building block can form strong cation- $\pi$  interactions with the planar TDPP moiety, leading to smaller intermolecular  $\pi$ - $\pi$  distance and extraordinary ion diffusion/injection behaviors. The cationic building block enhances the hydrophilicity and ionic-electronic coupling efficiency of the polymer backbone, leading to fast on/off response times of 1.00 ms/0.18 ms, while maintaining a high  $\mu C^*$  value of  $62.3 \text{ F}^{-1} \text{ cm}^{-1} \text{ V}^{-1} \text{ s}^{-1}$ . More importantly, after being reduced, the cationic backbone changes to a neutral backbone, which may benefit morphological stability and thereby device operational stability. These results demonstrate the great potential of using a cationic backbone for n-type OMIEC materials.

## Results and Discussion

### Polymer Design and Synthesis

Thiophene-flanked diketopyrrolopyrrole (TDPP) was chosen as the building block for this study because it is cheap and has good charge transport properties due to its planar backbone.<sup>[34]</sup> Compared with other naphthalene derivatives,

such as quinoline, fluoronaphthalene, and naphthonitrile, AN shows much lower calculated LUMO energy levels due to its cationic backbone (Figure 1b). To date, almost all the TDPP-based conjugated polymers show p-type or ambipolar OECT behaviors due to the high LUMO energy levels.<sup>[8,35–36]</sup> The low LUMO energy level of AN is promising for building an n-type TDPP polymer.

The synthesis of the AN and the polymers are shown in Figure 2. Ethyl 5-bromopicolinate was reacted with 1,4-butyrolactone via ester condensation, yielding compound 2. Compound 2 has a chiral center but both isomers were reactive in a proton-catalyzed decarboxylation-cyclization reaction, yielding compound 3. Compound 3 was dissolved in hydrobromic acid and brominated with liquid bromine. Compound 4 went through a dehydration process, giving AN a good yield. The existence of counterion  $\text{Br}^-$  was evaluated by iontophoresis, and only one major peak (95 % area of all anions) was observed (Figure. S1), confirming the high purity of the monomer. TDPP was grafted with heptaethylene glycol methyl ether (mPEG7,  $\text{R}_1$ ) and branched ethylene glycol ( $\text{R}_2$ ) as the side chains.<sup>[36–37]</sup> The branched side chain was employed to further optimize the device performance due to its better hydrophilicity. The ditributyltin-TDPP was prepared through lithium diisopropyl amide (LDA) deprotonation and  $\text{SnBu}_3\text{Cl}$  nucleophilic substitution, giving the TDPP tin reagent a purple liquid. The tin reagent was then used immediately for Stille polymerization. The dibromo-AN is soluble in water and common polar solvents (e.g. DMF). To enhance the polymerization efficiency, we used DMF as the cosolvent for polymerization. The resulting polymer, Poly-4a-Azonia-Naphthalene-thiophene-Diketopyrrolopyrrole with Anion (PANDA) is a dark green solid and soluble in chloroform. Interestingly, both monomers, the dibromo AN (3) and the TDPP monomer (8) are soluble in water, but the polymer PANDA is not water-soluble, suggesting the strong intermolecular interactions between the repeating units (Figure S2). For comparison, we also synthesized an isoelectronic polymer, Poly-Naphthalene-thiophene-Diketopyrrolopyrrole (PNPD), which has an almost identical backbone except for one atom. The molecular weight of both polymers was evaluated by gel permeation chromatography (GPC). All the polymers showed high molecular weights with  $M_n$  in the range of  $25.1\text{--}46.4 \text{ kg mol}^{-1}$  and PDI in the range of 1.51–1.76. We also carried out thermogravimetric analysis, PANDA and PANDA2 showed relatively lower degradation temperatures than PNPD, probably due to the evaporation of bromide ions<sup>[38]</sup> (Figure S3).

We evaluated the  $\pi$ - $\pi$  interactions between naphthalene (NP), AN and TDPP by density functional theory (DFT) calculations. The TDPP-AN complex shows larger binding energy ( $22.1 \text{ kcal mol}^{-1}$ ) than the TDPP-NP complex ( $13.4 \text{ kcal mol}^{-1}$ ), which could be attributed to the additional cation- $\pi$  interactions (Figure 3a, Table S1).<sup>[39]</sup> To find the optimized structure, we chose seven initial structures and performed structure optimization. After DFT optimization, five structures with local minimum energy were found (Figure S4). We found that when the bromide ion is close to the hydrogen atoms, the energy is the lowest, which could

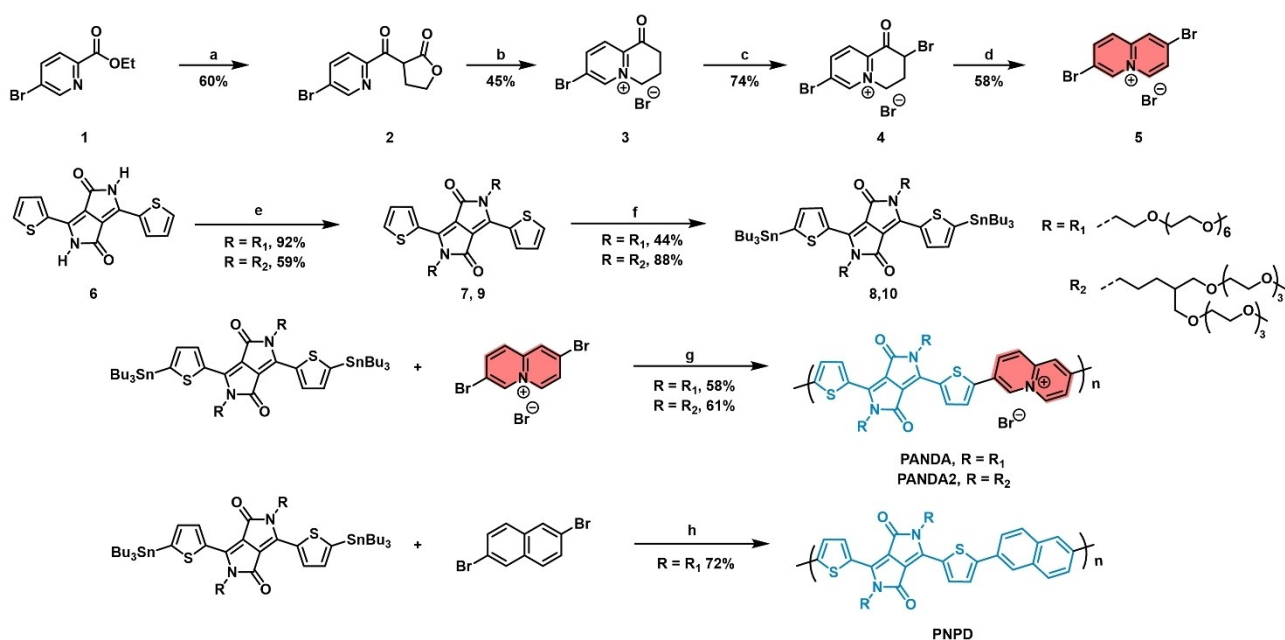


**Figure 2.** Synthetic route to AN and the polymers. Reagents and conditions a) NaH (1.1 eq.), THF, 1,4-butyrolactone (1.1 eq.), toluene, reflux, 8 h, 60%. b) 48% HBr, reflux, 1 h, then dichloroethane, heating, 45%. c) 48% HBr, Br<sub>2</sub> (1.1 eq.), reflux, 4 h, 74%. d) Ac<sub>2</sub>O, reflux, 3 h, 58%. e) RBr (2.2 eq.), 18-crown-6 (0.04 eq.), K<sub>2</sub>CO<sub>3</sub> (2.0 eq.), NMP, 130 °C, R = R<sub>1</sub>, 92%; R = R<sub>2</sub>, 59%. f) LDA (2.2 eq.), SnBu<sub>3</sub>Cl (2.2 eq.), THF, -110 °C to room temperature (RT), R = R<sub>1</sub>, 44%; R = R<sub>2</sub>, 88%. g) Pd(PPh<sub>3</sub>)<sub>4</sub> (0.04 eq.), CuI (0.04 eq.), DMF:CB=1, 135 °C, R = R<sub>1</sub>, 58%; R = R<sub>2</sub>, 61%. h) Pd(PPh<sub>3</sub>)<sub>4</sub> (0.04 eq.), CuI (0.04 eq.), DMF:CB=1, 135 °C, 8 h, 72%.

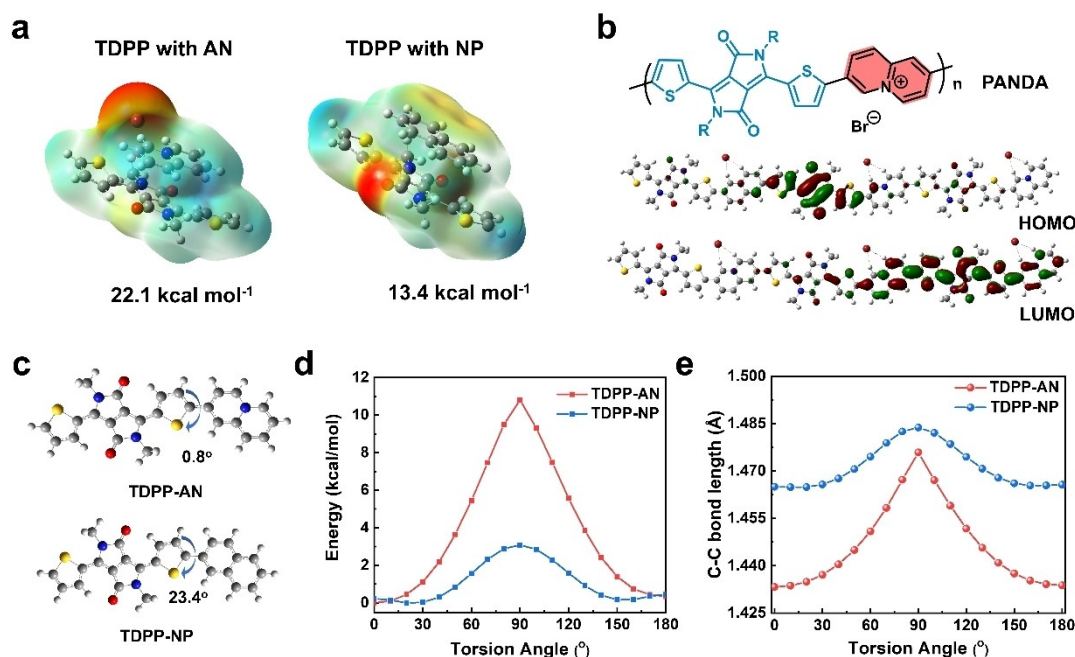


**Figure 3.** DFT calculations of the polymers. a) DFT-calculated cation- $\pi$  interaction between AN bromide and TDPP, compared with the interaction between naphthalene and TDPP. ( $\omega$ B97XD/6-311g(d,p), with BSSE correction). b) Polymer structure and molecular frontier orbitals of PANDA. We omitted the orbitals on the Br<sup>-</sup>. c) DFT-optimized molecular structures of TDPP-AN and TDPP-NP monomers (B3LYP/6-311g(d,p)). d) Comparison of the relaxed potential energy surface (PES) scan of the TDPP-AN and TDPP-NP torsion angle as indicated in Figure 3c. e) Comparison of the bond length changes as the torsional angle changing for TDPP-AN and TDPP-NP.

be due to the hydrogen bonds between the bromide ion and the nearby hydrogen atoms. DFT study shows that PANDA has a more planar backbone conformation, while PNPD has

a larger dihedral angle (Figure 3c). To understand this difference, we carried out a relaxed potential energy surface (PES) scan of the torsional angles between the TDPP and

AN/NP moieties. As shown in Figure 3d, TDPP-AN has a rotational barrier as high as 11 kcalmol<sup>-1</sup>; while for TDPP-NP, the barrier is only 3 kcalmol<sup>-1</sup>. To our knowledge, such a high rotational barrier is seldom observed in conjugated polymers. Further theoretical analysis suggests that the high rotation barrier is largely due to the strong electron-withdrawing property of AN, making more electrons originally on thiophene distribute onto AN moiety (Figure S9). This charge redistribution could shorten the bond length between thiophene and AN (Figure 3e). The bond length of TDPP and AN unit is 1.44 Å, between a typical single bond and a double bond (see more detailed analysis in Figure S7–S10). In addition, the HOMO of PANDA is localized on the TDPP moiety, whereas the LUMO is delocalized along the polymer backbone (Figure 3b). Compared with PANDA, both the frontier orbitals of PNPD are delocalized (Figure S6). These results suggest that cationic building blocks could bring new molecular features (e.g. better backbone planarity, higher rotational barrier, and different frontier orbital distributions) rather than simply lowering LUMO energy levels.

### Understanding of the Cation- $\pi$ Interactions

OMIECs are usually operated in aquatic environment, so we studied AN and TDPP interactions in D<sub>2</sub>O using solution <sup>1</sup>H NMR. TDPP is dissolved in D<sub>2</sub>O at a concentration of 16.2 mM. By increasing the AN from 0 to 18.6 mM, we observed clear changes in the chemical shift of all the H on TDPP. Among them, H<sub>a</sub> and H<sub>b</sub> shifted to a lower field (higher radiation frequency, Hz), whereas H<sub>c</sub> shifted to a higher field (lower frequency) (Figure 4b). This indicates that H<sub>c</sub> is strongly shielded by AN while the other two H on thiophene are deshielded. To exclude the potential effects caused by anions, we added tetra-*n*-butylammonium bromide (Bu<sub>4</sub>N<sup>+</sup>Br<sup>-</sup>) to the TDPP solution. As shown in Figure 4c, we only observed slightly deshielding effects caused by the Br<sup>-</sup>, which may originate from the weak Br<sup>-</sup>...H interactions. Control experiments also show that salts with different anions have weak effects on the NMR spectra (Figure S11). Thus, the large chemical shifts are caused by the cations, not by the anions. This shielding and deshielding effect can be well understood by our optimized AN-TDPP molecular packing model (Figure 4a). When AN is on top of TDPP, H<sub>c</sub> is under AN, leading to the shielding effect; while H<sub>a</sub> and H<sub>b</sub> are outside of the AN covered area, resulting deshielding effect. We use chemical shift change per concentration (Hz mM<sup>-1</sup>) to describe the interaction of

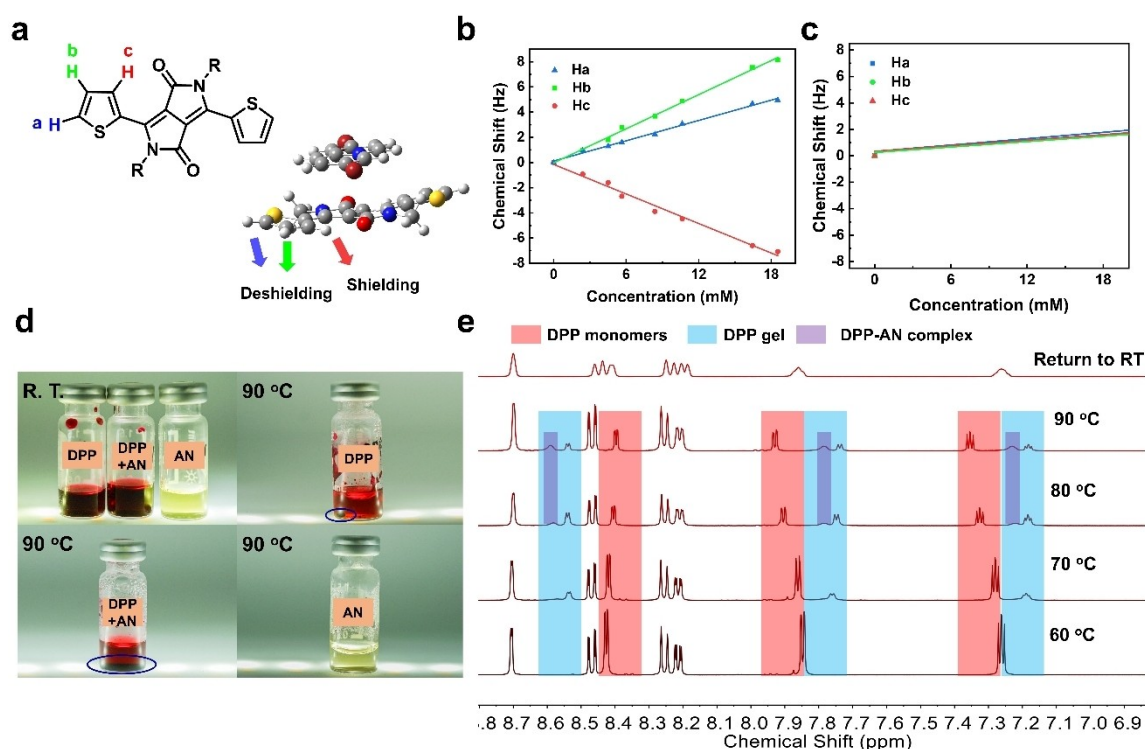


**Figure 4.** Understanding of the cation- $\pi$  interactions between TDPP and AN. a) TDPP structure and the optimized molecular packing model of AN-TDPP complex. b) Chemical shift changes of TDPP after adding 0, 2.43, 4.54, 5.67, 8.42, 10.7, 16.5, 18.6 mM AN in D<sub>2</sub>O, the concentration of TDPP is 16.2 mM. c) Chemical shift changes of TDPP after adding 0 to 100 mM TBAB in D<sub>2</sub>O. See the full concentration range in Figure S11. The TDPP concentration is also 16.2 mM. d) The phase separation of TDPP solution during heating. TDDP, AN, and TDPP + AN show good solubility in water at RT. TDPP forms a drop of oil at 90 °C, suggesting the aggregation of TDPP. TDPP + AN forms amorphous precipitates at 90 °C. AN solution is clear at 90 °C. e) Variable-temperature (VT) <sup>1</sup>H NMR of TDPP and AN mixture (1:1 molar ratio).

TDPP with thiophene-carbonitrile and naphthalene (Figure S12). These results show AN has a much stronger interaction with TDPP than naphthalene or cyano-substituted thiophene. We also carried out temperature-variable  $^1\text{H}$  NMR experiments (Figure 4e). For TDPP in water, new peaks emerge above  $70^\circ\text{C}$  due to the aggregation of the TDPP (Figure S14). Since higher temperature can destroy the hydrogen bonds between the EG side chains and water,<sup>[40]</sup> the solubility of TDPP starts to decrease and result in aggregates formation (Figure 4d, TDPP at  $90^\circ\text{C}$ , blue circle). After adding AN to the TDPP solution (1:1 molar ratio) and raising the temperature above  $70^\circ\text{C}$ , except for the TDPP aggregates' peaks, a new set of peaks appeared, which can be attributed to the AN-TDPP complex (Figure 4e). The new peaks are broadened, suggesting that the AN-TDPP might adopt different packing conformations. After cooling to room temperature, the AN-TDPP formed some precipitates, further confirming the formation of the AN-TDPP complex (Figure 4d, blue circle). All the above results demonstrate that the cationic AN indeed forms strong cation- $\pi$  interactions with TDPP in water.

To explore the cation- $\pi$  interactions in solid state, we performed the solid-state NMR using  $^{13}\text{C}$  high-power decoupling with magic angle spinning (HPDec-MAS) technique for the monomers (Figure S15). The HPDec-MAS experiment excites all nuclei non-selectively and the integration of the peak is related to the carbon content. All samples are dispersed in inertia silica, and the chemical shifts ( $\delta$  ppm) were determined to an internal standard. With the addition of AN to DPP, the peaks in the range of 120–140 ppm raised dramatically, while the peaks between 55 ppm and 78 ppm remain unchanged. When mixed with DPP, the peak of AN at 110 ppm disappear and most of the AN peaks shifted clearly. Combining all the data, we can conclude that DPP has a strong interaction with AN in solid state. The shielding effect of the DPP caused the disappearance and the shift of the C atoms on AN and these effects happened only on the aromatic core due to the cation- $\pi$  interactions, since the C atoms of the side chains are less affected.

### Electrochemical Properties and OECT Device Performance

We measured and calculated the UV/Vis absorption spectra of PANDA and PNPd to understand their electronic properties (Figure 5a, b, and Figure S16–S18). The absorption onset of PANDA is 979 nm in solution, and 1076 nm in solid state (Figure 5a). After going from solution to solid state, both polymers showed redshifted spectra due to the backbone planarization and polymer aggregation in the solid state. Compared with PNPd (Figure 5b, 778 nm to 931 nm), the shift of PANDA is smaller, suggesting that PANDA has a more planar backbone conformation in solution. This is supported by the above DFT calculations that the rotational barrier between AN and TDPP is higher than NP and TDPP, and the most stable conformation of TDPP-AN is at  $0.8^\circ$ . Thus, AN provides PANDA with a more planar and

rigid backbone, which will benefit intrachain and interchain charge transport.

The redox properties of the two polymers were measured by cyclic voltammetry (CV). The measured LUMO energy level of PANDA ( $-4.21$  eV) is much lower than that of PNPd ( $-3.78$  eV), consistent with the DFT calculations (Table S2, Figure S19). Compared with other TDPP-based polymers, PANDA has the lowest LUMO energy levels.<sup>[41]</sup> Continuous CV sweeps of two polymers were explored in 0.1 M NaCl solution. Both PANDA and PNPd show good stability in the cycling test with small current decay, suggesting their good electrochemical stability (Figure S20). To investigate the electrochemical characteristics of both polymers, spectroelectrochemistry was performed. PANDA is electrochemically doped since bias at  $-0.3$  V and fully doped at  $-0.8$  V, while PNPd requires higher positive voltages over  $+1.0$  V to oxidize (Figure 5c, d). This indicates that PANDA can be readily reduced and is a typical n-type material, while PNPd is a p-type material. The polaron peaks of both polymers raised and the original peak decreased, exhibiting a typical electrochemically doping process. The polaron peak of PANDA ( $>1000$  nm) is much stronger than that of PNPd ( $>800$  nm), suggesting that PANDA could exhibit satisfactory n-type OECT performances.<sup>[42]</sup> The results aligned with our expectations. Specifically, PNPd shows a typical p-type OECT performance with a low  $\mu C^*$  of  $0.262$   $\text{F cm}^{-1} \text{V}^{-1} \text{s}^{-1}$  (Figure S21 and Table 1), which is probably due to its non-planar backbone and high oxidation potential. In comparison, PANDA shows n-type OECT behaviors. The introduction of cationic fragments effectively lowers the LUMO level, yielding n-type polymers. The normalized transconductance ( $g_{m,\text{norm}}$ ) of PANDA is  $14.7$   $\text{Scm}^{-1}$  and the calculated  $\mu C^*$  is up to  $40.7$   $\text{F cm}^{-1} \text{V}^{-1} \text{s}^{-1}$ . For PANDA2 with branched EG chains,  $g_{m,\text{norm}}$  reaches  $19.3$   $\text{Scm}^{-1}$ , and  $\mu C^*$  reaches  $62.3$   $\text{F cm}^{-1} \text{V}^{-1} \text{s}^{-1}$  (Figure 5e, f Table S3). Furthermore, a high-performance p-type polymer P(bgDPP-MeOT2)<sup>[37]</sup> was employed to fabricate complementary inverters with PANDA. When the supply voltage ( $V_{\text{DD}}$ ) is set to  $0.5$  V and the input voltage ( $V_{\text{in}}$ ) is swept from  $0$  to  $0.5$  V, a record high gain value ( $\partial V_{\text{out}}/\partial V_{\text{in}}$ ) of  $71$  at  $0.5$  V is obtained (Figure 5g, Table S4). Although vertical OECTs could show even higher gain up to  $150$  at  $0.7$  V, our devices show the best gain in planar OECT devices.<sup>[43]</sup> The inverter also shows very small

**Table 1:** Summary of the OECT performance of the two polymers.

Polymer	$g_{m,\text{norm}}$ <sup>[a]</sup> ( $\text{Scm}^{-1}$ )	$V_{\text{th}}$ <sup>[b]</sup> (V)	$\mu C^*$ <sup>[c]</sup> ( $\text{F cm}^{-1} \text{V}^{-1} \text{s}^{-1}$ )	$\mu$ <sup>[d]</sup> ( $\text{cm}^2 \text{V}^{-1} \text{s}^{-1}$ )	$C^*$ ( $\text{F cm}^{-3}$ )
PANDA	14.7	0.44	40.7 ( $39.6 \pm 1.6$ )	0.23	$181 \pm 19$
PANDA2	19.2	0.47	62.3 ( $51.4 \pm 6.8$ )	0.33	$197 \pm 8$
PNPD	0.0445	$-0.67$	0.262 ( $0.232 \pm 0.022$ )	0.0019	$137 \pm 26$

[a] The  $W/L$  of all devices is  $100/10$   $\mu\text{m}$ . All of the OECT devices were operated in a  $0.1$  M NaCl aqueous solution. [b]  $V_{\text{th}}$  was determined by extrapolating the corresponding  $I_{\text{DS}}^{1/2}$  versus  $V_{\text{GS}}$  plots. [c] The data outside the brackets are maximal data, and the inside ones are the average. [d]  $\mu$  was calculated from  $\mu C^*$  and the measured volumetric capacitance  $C^*$ . PNPd is a p-type polymer. Several devices were tested and computed for each polymer (see details in Table S3).

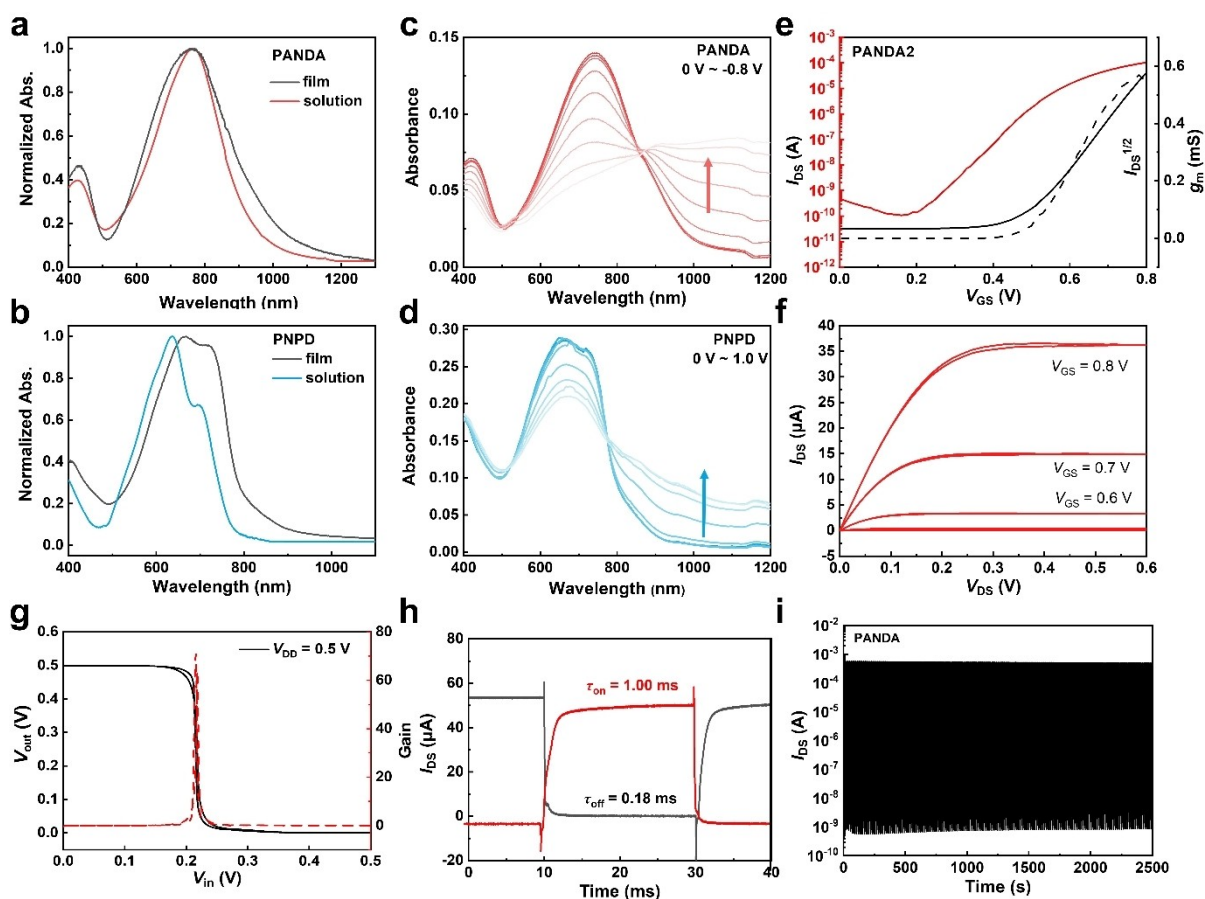


**Figure 5.** Optoelectronic properties and OECT device characterization. a) and b) Absorption spectra of PANDA & PNPD. c) and d) Electrochemical spectra of PANDA & PNPD. e) Transfer characteristics of PANDA2. f) Output characteristic of PANDA2.  $V_{DS} = 0.6$  V,  $W/L = 100/10$   $\mu\text{m}$ . g) Voltage transfer characteristics and gain of the complementary inverter based on PANDA and P(bgDPP-MeOT2). h) Transient response of PANDA2. i) Long-term on-off switching of PANDA.  $V_{DS} = 0.6$  V; a gate voltage pulse  $V_{GS} = 0.8$  V;  $W/L = 100/10$   $\mu\text{m}$ .

hysteresis and rail-to-rail voltage swings, with performance a comparable to the OECT-based inverters employing inorganic IGZO as the n-channel material.<sup>[44]</sup>

We measured the capacitance of the OECT device by electrochemical impedance spectroscopy (EIS) and found that the  $C^*$  is  $181 \text{ F cm}^{-3}$  for PANDA and  $197 \text{ F cm}^{-3}$  for PANDA2 (Figure S23). These values are higher than that of PNPD ( $137 \text{ F cm}^{-3}$ ), probably due to hydrophilicity of the cationic backbone. The mobilities are calculated to be  $0.23$  and  $0.33 \text{ cm}^2 \text{ V}^{-1} \text{ s}^{-1}$  for PANDA and PANDA2, respectively. PANDA also shows a fast response speed of  $\tau_{\text{on}}/\tau_{\text{off}} = 2.34/0.30$  ms (Figure S22), and PANDA2 shows an even faster response speed of  $\tau_{\text{on}}/\tau_{\text{off}} = 1.00/0.18$  ms (Figure 5h).<sup>[24–25,35]</sup> We relate the high response speed to its hydrophilic cationic backbones and high electron mobility. The hydrophilic backbone allows fast ion diffusions, and the high electron mobility guarantees fast charge transport between source-drain electrodes. Thus, PANDA is a promising material for real-time high-speed sensing applications. PANDA also shows high stability under on-off cycling with a current retention of 89% after 2500 s operation in the air (Figure 5i).<sup>[45–46]</sup> This is better than its hydrophobic counterparts, P(gTDPP2FT) (61% retention after 2500 s cycling),

and other recently reported n-type materials, such as f-BTI2 g-TVTCN (75% current retention after 2400 s cycling).<sup>[25,36]</sup> In comparison, PNPD shows poor operation stability, probably due to its low HOMO energy level, making the polymer cannot be easily oxidized (Figure S27). Therefore, the cationic hydrophilic fragment improves the volumetric capacitance and the strong cation- $\pi$  interaction of AN enables high charge carrier mobility under doped conditions. All the features endow PANDA with high mixed ionic-electronic coupling efficiency and thereby better OECT device performances. To explore the generality of incorporating AN for other polymers, we performed DFT calculations. After incorporating AN, all the polymers show significantly lowered LUMO levels in the range of  $-3.61$  to  $-4.24$  eV. The LUMO levels lowered by  $0.47$ – $1.71$  eV due to AN's strong electron deficiency. Therefore, AN can greatly lower the LUMO levels of conjugated polymers and might be a general choice for other types of n-type polymers (Figure S28 and related discussions).

## Film microstructure characterization

Grazing incidence wide-angle X-ray scattering (GIWAXS) and atomic force microscope (AFM) were employed to explore the molecular packing and film morphology. PANDA shows a face-on molecular packing, while PNPd shows an edge-on packing (Figure 6a, b). The lamellar distance of PANDA is 30.1 Å, larger than that of PNPd (24.2 Å). The larger lamellar distance might correspond to the bromide counterions inserted into the glycol side chains. Notably, PANDA has a  $\pi$ - $\pi$  stacking distance of 3.59 Å, shorter than that of PNPd (3.65 Å), which could be attributed to the cation- $\pi$  interaction in PANDA. This change suggests a stronger interchain interactions. Compared to PNPd, PANDA has a smaller persistent length and larger paracrystalline disorder ( $g$  value) (Table S5), suggesting that PANDA has lower crystallinity and poor molecular order in solid state. The lower crystallinity of PANDA is probably due to the interference of the bromide counterions (Table S6). We also measured the GIWAXS of the polymer film after being exposed to aqueous media and electrochemically doped. The scattering of PANDA film showed no obvious change after exposure to the electrolyte. After being reduced, the  $\pi$ - $\pi$  stacking peak (010) becomes stronger and the  $\pi$ - $\pi$  stacking distance becomes smaller (3.59 Å to 3.51 Å), suggesting that the molecular packing of PANDA becomes a little bit more ordered with even smaller interchain distance (Figure 6c). In contrast, after being exposed and oxidized, the scattering of the PNPd film showed weaker lamellar and the  $\pi$ - $\pi$  stacking distance becomes larger (3.65 Å to 3.66 Å) (Figure 6d). We attribute the decrease of the  $\pi$ - $\pi$  stacking distance after reducing to the cationic backbone of PANDA. After reducing the polymer, some cationic units become neutral and the bromides move

farther from the backbone, which might reduce bromides' disturbance on interchain  $\pi$ - $\pi$  stacking, leading to closer  $\pi$ - $\pi$  stacking distances. Note that after exposing and reducing, the lamellar distances become larger, suggesting that the water and ions go into the side chain region without disrupting the  $\pi$ - $\pi$  stacking. These results demonstrate that polymers with cationic backbones can have morphology changes that can benefit charge transport during water uptake and ion injection/extraction, leading to more stable device cycling performance.

Both polymer films are smooth with small root-mean-square (RMS) roughness in AFM height images (Figure S29). PANDA has fiber-like networks with smaller grain sizes than PNPd, consistent with the smaller persistent length of PANDA. After being exposed to water and electrochemical doping, both polymers show small morphological changes, and the roughness of the films is slightly increased. All these results seem to contradict the good charge transport property of PANDA since polymers with higher crystallinity often exhibit better charge transport properties.<sup>[47]</sup> However, recent studies have shown that molecular packing order is not the most important parameter for high-mobility conjugated polymers, and good intrachain charge transport and interchain short-range contacts are more critical.<sup>[48–49]</sup> PANDA has a more planar backbone and a smaller  $\pi$ - $\pi$  stacking distance. Its planar backbone allows faster intrachain transport, and the smaller  $\pi$ - $\pi$  stacking distance guarantees efficient interchain charge transport. Both features originate from its cationic backbone.

To further understand the film changes after being exposed to electrolyte and doping, we performed electrochemical quartz crystal microbalance with dissipation (EQCM-D) measurements. We found that PANDA showed interesting water absorption and ion diffusion/injection characteristics (Figure S30). PNPd showed passive swelling of 61.4 % (exposed to 0.1 M NaCl), and an active swelling of 6.3 % (electrically biased at +0.9 V vs. Ag/AgCl). An n-type polymer P(gTDPP2FT) exhibited passive swelling of 113 %, and an active swelling (biased at -0.9 V) of 1.3 %.<sup>[36]</sup> However, PANDA showed huge passive swelling of 153 %, but no obvious active swelling (biased at -0.8 V). We propose that the unique swelling characteristics of PANDA result from its cationic structure. The  $\text{Na}^+ \cdot x\text{H}_2\text{O}$  will penetrate into the film, while the  $\text{Br}^- \cdot y\text{H}_2\text{O}$  will go out at the same time (Figure S31). The mass changes are just in balance and EQCM-D shows no net mass change. However, for polymers with a neutral backbone (for both p- and n-type polymers), there must be an obvious mass change during oxidation/reduction, which could lead to device instability.<sup>[50]</sup>

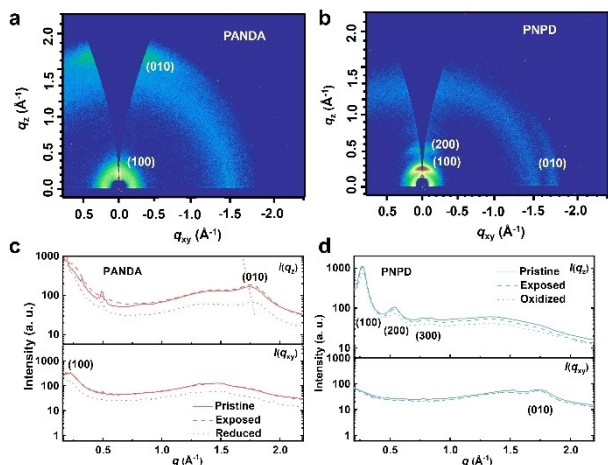


**Figure 6.** Molecular packing and morphology characterization. a) and b) 2D-GIWAXS of PANDA and PNPd in their pristine films. c) and d) Line cuts along the  $q_y$  direction represent scattering in the in-plane direction, while the  $q_z$  is from the out-of-plane direction. “Pristine” stands for dry films without any treatment. “Exposed” stands for the films immersed in 0.1 M NaCl for 10 min and blow-dried. “Oxidized/Reduced” stands for the films on the silicon substrate that are oxidized/reduced by voltage bias for 10 min and blow-dried.

## Conclusion

In summary, we have developed a cationic building block, namely AN, for constructing n-type conjugated polymers. AN has a simple structure but with unprecedentedly strong electron-withdrawing properties. We found that water-

soluble cationic AN can form strong  $\pi$ - $\pi$  stacking interactions with water-soluble TDPP via cation- $\pi$  interactions. The strong underwater cation- $\pi$  interactions physically cross-linked the polymer, making it insoluble in water and leading to a shorter  $\pi$ - $\pi$  stacking distance, high electron mobility, and good morphology stability. In addition, the cationic backbone also enhances hydrophilicity, leading to high volumetric capacitance, faster ion diffusion/injection, and better operational stability. Different from conventional polymer design focusing on the synthesis of polymers with neutral backbones, our work demonstrates a new approach using ionic backbones for next-generation organic electronic materials working in aqueous media.

### Supporting Information

The authors declare that the data supporting the findings of this study are available within the paper and its Supporting Information files.

### Acknowledgements

This work is supported by the National Key R&D Program of China (2022YFE0130600) and the National Natural Science Foundation of China (22075001 and 92156019). The computational part is supported by the High-Performance Computing Platform of Peking University. We acknowledge the Molecular Materials and Nanofabrication Laboratory (MMNL) in the College of Chemistry and Electron Microscopy Laboratory of Peking University for the use of instruments. We thank beamline BL14B1 (Shanghai Synchrotron Radiation Facility) for providing beamtime for part of the XRD study. We thank the support from Clinical Medicine Plus X - Young Scholars Project, Peking University, the Fundamental Research Funds for the Central Universities.

### Conflict of Interest

The authors declare no conflict of interest.

### Data Availability Statement

The data that support the findings of this study are available from the corresponding author upon reasonable request.

**Keywords:** Cation- $\pi$  Interaction · Cationic Building Block · Organic Electrochemical Transistor · Organic Mixed Ionic-Electronic Conductor · n-Type Conjugated Polymer

[1] B. D. Paulsen, K. Tybrandt, E. Stavrinidou, J. Rivnay, *Nat. Mater.* **2020**, *19*, 13–26.

- [2] P. C. Harikesh, C.-Y. Yang, H.-Y. Wu, S. Zhang, M. J. Donahue, A. S. Caravaca, J.-D. Huang, P. S. Olofsson, M. Berggren, S. Fabiano, *Nat. Mater.* **2023**, *22*, 242–248.
- [3] Z. Zhang, W. Wang, Y. Jiang, Y.-X. Wang, Y. Wu, J.-C. Lai, S. Niu, C. Xu, C.-C. Shih, C. Wang, H. Yan, L. Galuska, N. Prine, H.-C. Wu, D. Zhong, G. Chen, N. Matsuhisa, Y. Zheng, Z. Yu, Y. Wang, R. Dauskardt, X. Gu, J. B. H. Tok, Z. Bao, *Nature* **2022**, *603*, 624–630.
- [4] W. Lee, S. Kobayashi, M. Nagase, Y. Jimbo, I. Saito, Y. Inoue, T. Yambe, M. Sekino, G. G. Malliaras, T. Yokota, M. Tanaka, T. Someya, *Sci. Adv.* **2018**, *4*, eaau2426.
- [5] P. Lin, F. Yan, *Adv. Mater.* **2012**, *24*, 34–51.
- [6] J. Rivnay, S. Inal, A. Salleo, R. M. Owens, M. Berggren, G. G. Malliaras, *Nat. Rev. Mater.* **2018**, *3*, 17086.
- [7] A. Giovannitti, D.-T. Sbircea, S. Inal, C. B. Nielsen, E. Bandiello, D. A. Hanifi, M. Sessolo, G. G. Malliaras, I. McCulloch, J. Rivnay, *Proc. Natl. Acad. Sci. USA* **2016**, *113*, 12017–12022.
- [8] M. Moser, A. Savva, K. Thorley, B. D. Paulsen, T. C. Hidalgo, D. Ohayon, H. Chen, A. Giovannitti, A. Marks, N. Gasparini, A. Wadsworth, J. Rivnay, S. Inal, I. McCulloch, *Angew. Chem. Int. Ed.* **2021**, *60*, 7777–7785.
- [9] M. Moser, T. C. Hidalgo, J. Surgailis, J. Gladisch, S. Ghosh, R. Sheelamanthula, Q. Thiburce, A. Giovannitti, A. Salleo, N. Gasparini, A. Wadsworth, I. Zozoulenko, M. Berggren, E. Stavrinidou, S. Inal, I. McCulloch, *Adv. Mater.* **2020**, *32*, e2002748.
- [10] R. K. Hallani, B. D. Paulsen, A. J. Petty, R. Sheelamanthula, M. Moser, K. J. Thorley, W. Sohn, R. B. Rashid, A. Savva, S. Moro, J. P. Parker, O. Drury, M. Alsufyani, M. Neophytou, J. Kosco, S. Inal, G. Costantini, J. Rivnay, I. McCulloch, *J. Am. Chem. Soc.* **2021**, *143*, 11007–11018.
- [11] X. Luo, H. Shen, K. Perera, D. T. Tran, B. W. Boudouris, J. Mei, *ACS Macro Lett.* **2021**, *10*, 1061–1067.
- [12] L. Lan, J. Chen, Y. Wang, P. Li, Y. Yu, G. Zhu, Z. Li, T. Lei, W. Yue, I. McCulloch, *Chem. Mater.* **2022**, *34*, 1666–1676.
- [13] Y. Kim, H. Noh, B. D. Paulsen, J. Kim, I.-Y. Jo, H. Ahn, J. Rivnay, M.-H. Yoon, *Adv. Mater.* **2021**, *33*, e2007550.
- [14] S.-M. Kim, C.-H. Kim, Y. Kim, N. Kim, W.-J. Lee, E.-H. Lee, D. Kim, S. Park, K. Lee, J. Rivnay, M.-H. Yoon, *Nat. Commun.* **2018**, *9*, 3858–3866.
- [15] C. Cea, G. D. Spyropoulos, P. Jastrzebska-Perfect, J. J. Ferrero, J. N. Gelinis, D. Khodagholy, *Nat. Mater.* **2020**, *19*, 679–686.
- [16] S. Inal, G. G. Malliaras, J. Rivnay, *Nat. Commun.* **2017**, *8*, 1767–1773.
- [17] A. Giovannitti, C. B. Nielsen, D.-T. Sbircea, S. Inal, M. Donahue, M. R. Niazi, D. A. Hanifi, A. Amassian, G. G. Malliaras, J. Rivnay, I. McCulloch, *Nat. Commun.* **2016**, *7*, 13066–13074.
- [18] A. Giovannitti, I. P. Maria, D. Hanifi, M. J. Donahue, D. Bryant, K. J. Barth, B. E. Makdah, A. Savva, D. Moia, M. Zetek, P. R. F. Barnes, O. G. Reid, S. Inal, G. Rumbles, G. G. Malliaras, J. Nelson, J. Rivnay, I. McCulloch, *Chem. Mater.* **2018**, *30*, 2945–2953.
- [19] H. Sun, M. Vagin, S. Wang, X. Crispin, R. Forchheimer, M. Berggren, S. Fabiano, *Adv. Mater.* **2018**, *30*, 1704916.
- [20] X. Chen, A. Marks, B. D. Paulsen, R. Wu, R. B. Rashid, H. Chen, M. Alsufyani, J. Rivnay, I. McCulloch, *Angew. Chem. Int. Ed.* **2021**, *60*, 9368–9373.
- [21] A. Marks, X. Chen, R. Wu, R. B. Rashid, W. Jin, B. D. Paulsen, M. Moser, X. Ji, S. Griggs, D. Meli, X. Wu, H. Bristow, J. Strzalka, N. Gasparini, G. Costantini, S. Fabiano, J. Rivnay, I. McCulloch, *J. Am. Chem. Soc.* **2022**, *144*, 4642–4656.
- [22] D. Moia, A. Giovannitti, A. A. Szumska, I. P. Maria, E. Rezasoltani, M. Sachs, M. Schnurr, P. R. F. Barnes, I. McCulloch, J. Nelson, *Energy Environ. Sci.* **2019**, *12*, 1349–1357.

- [23] Z. S. Parr, J. Borges-González, R. B. Rashid, K. J. Thorley, D. Meli, B. D. Paulsen, J. Strzalka, J. Rivnay, C. B. Nielsen, *Adv. Mater.* **2022**, *34*, e2107829.
- [24] K. Feng, W. Shan, S. Ma, Z. Wu, J. Chen, H. Guo, B. Liu, J. Wang, B. Li, H. Y. Woo, S. Fabiano, W. Huang, X. Guo, *Angew. Chem. Int. Ed.* **2021**, *60*, 24198–24205.
- [25] K. Feng, W. Shan, J. Wang, J.-W. Lee, W. Yang, W. Wu, Y. Wang, B. J. Kim, X. Guo, H. Guo, *Adv. Mater.* **2022**, *34*, e2201340.
- [26] W. Yang, K. Feng, S. Ma, B. Liu, Y. Wang, R. Ding, S. Y. Jeong, H. Y. Woo, P. K. L. Chan, X. Guo, *Adv. Mater.* **2023**, <https://doi.org/10.1002/adma.202305416>.
- [27] J. Shi, P. Li, X.-Y. Deng, J. Xu, Z. Huang, Y. Lei, Y. Wang, J.-Y. Wang, X. Gu, T. Lei, *Chem. Mater.* **2022**, *34*, 864–872.
- [28] Y. Wang, E. Zeglio, L. Wang, S. Cong, G. Zhu, H. Liao, J. Duan, Y. Zhou, Z. Li, D. Mawad, A. Herland, W. Yue, I. McCulloch, *Adv. Funct. Mater.* **2022**, *32*, 2111439.
- [29] Y. Wang, A. Koklu, Y. Zhong, T. Chang, K. Guo, C. Zhao, T. C. H. Castillo, Z. Bu, C. Xiao, W. Yue, W. Ma, S. Inal, *Adv. Funct. Mater.* **2023**, <https://doi.org/10.1002/adfm.202304103>.
- [30] N. Sagawa, T. Shikata, *Phys. Chem. Chem. Phys.* **2014**, *16*, 13262–13270.
- [31] D. Ohayon, A. Savva, W. Du, B. D. Paulsen, I. Uguz, R. S. Ashraf, J. Rivnay, I. McCulloch, S. Inal, *ACS Appl. Mater. Interfaces* **2021**, *13*, 4253–4266.
- [32] I. C. Gherghi, S. T. Girousi, A. N. Voulgaropoulos, R. Tzimou-Tsitouridou, *Talanta* **2003**, *61*, 103–112.
- [33] R. Galindo-Murillo, T. E. Cheatham, *Nucleic Acids Res.* **2021**, *49*, 3735–3747.
- [34] J. Yang, Z. Zhao, S. Wang, Y. Guo, Y. Liu, *Chem* **2018**, *4*, 2748–2785.
- [35] J. J. Samuel, A. Garudapalli, A. A. Mohapatra, C. Gangadharappa, S. Patil, N. P. B. Aetukuri, *Adv. Funct. Mater.* **2021**, *31*, 2102903.
- [36] P. Li, J. Shi, Y. Lei, Z. Huang, T. Lei, *Nat. Commun.* **2022**, *13*, 5970–5977.
- [37] H. Jia, Z. Huang, P. Li, S. Zhang, Y. Wang, J.-Y. Wang, X. Gu, T. Lei, *J. Mater. Chem. C* **2021**, *9*, 4927–4934.
- [38] S. Hwang, W. J. Potscavage, Y. S. Yang, I. S. Park, T. Matsushima, C. Adachi, *Phys. Chem. Chem. Phys.* **2016**, *18*, 29199–29207.
- [39] D. A. Dougherty, *Acc. Chem. Res.* **2013**, *46*, 885–893.
- [40] J. G. Morton, C. L. Joe, M. C. Stolla, S. R. Koshland, C. H. Londregan, M. H. Schofield, *J. Chem. Educ.* **2015**, *92*, 1086–1090.
- [41] Q. Liu, S. E. Bottle, P. Sonar, *Adv. Mater.* **2020**, *32*, 1903882.
- [42] J. Rivnay, P. Leleux, M. Sessolo, D. Khodagholy, T. Hervé, M. Flocchi, G. G. Malliaras, *Adv. Mater.* **2013**, *25*, 7010–7014.
- [43] W. Huang, J. Chen, Y. Yao, D. Zheng, X. Ji, L.-W. Feng, D. Moore, N. R. Glavin, M. Xie, Y. Chen, R. M. Pankow, A. Surendran, Z. Wang, Y. Xia, L. Bai, J. Rivnay, J. Ping, X. Guo, Y. Cheng, T. J. Marks, A. Facchetti, *Nature* **2023**, *613*, 496–502.
- [44] Y. Yao, W. Huang, J. Chen, G. Wang, H. Chen, X. Zhuang, Y. Ying, J. Ping, T. J. Marks, A. Facchetti, *Proc. Natl. Acad. Sci. USA* **2021**, *118*, e2111790118.
- [45] A. Giovannitti, R. B. Rashid, Q. Thiburce, B. D. Paulsen, C. Cendra, K. Thorley, D. Moia, J. T. Mefford, D. Hanifi, D. Weiyuan, M. Moser, A. Salleo, J. Nelson, I. McCulloch, J. Rivnay, *Adv. Mater.* **2020**, *32*, e1908047.
- [46] Y. Wang, E. Zeglio, H. Liao, J. Xu, F. Liu, Z. Li, I. P. Maria, D. Mawad, A. Herland, I. McCulloch, W. Yue, *Chem. Mater.* **2019**, *31*, 9797–9806.
- [47] T. C. Hidalgo Castillo, M. Moser, C. Cendra, P. D. Nayak, A. Salleo, I. McCulloch, S. Inal, *Chem. Mater.* **2022**, *34*, 6723–6733.
- [48] R. Noriega, J. Rivnay, K. Vandewal, F. P. V. Koch, N. Stingelin, P. Smith, M. F. Toney, A. Salleo, *Nat. Mater.* **2013**, *12*, 1038–1044.
- [49] X. Yan, M. Xiong, X.-Y. Deng, K.-K. Liu, J.-T. Li, X.-Q. Wang, S. Zhang, N. Prine, Z. Zhang, W. Huang, Y. Wang, J.-Y. Wang, X. Gu, S. K. So, J. Zhu, T. Lei, *Nat. Commun.* **2021**, *12*, 5723–5731.
- [50] L. Q. Flagg, C. G. Bischak, J. W. Onorato, R. B. Rashid, C. K. Luscombe, D. S. Ginger, *J. Am. Chem. Soc.* **2019**, *141*, 4345–4354.

Manuscript received: September 6, 2023

Accepted manuscript online: November 8, 2023

Version of record online: December 28, 2023